




 Cite this: *RSC Adv.*, 2024, 14, 10714

# UV-assisted synthesis of ultra-small GO–Austar for efficient PTT therapeutic architectonic construction†

 Ang Gao,<sup>‡,a</sup> Lijia Pei,<sup>‡,d</sup> Guan Liu,<sup>a</sup> Yunsheng Chen,<sup>c</sup> Amin Zhang <sup>\*ab</sup> and Daxiang Cui <sup>\*a</sup>

Conventional Au nanomaterial synthesis typically necessitates the involvement of extensive surfactants and reducing agents, leading to a certain amount of chemical waste and biological toxicity. In this study, we innovatively employed ultra-small graphene oxide as a reducing agent and surfactant for the *in situ* generation of small Au nanoparticles under ultraviolet irradiation (UV) at ambient conditions. After ultra-small GO–Au seeds were successfully synthesized, we fabricated small star-like Au nanoparticles on the surface of GO, in which GO effectively prevented Austar from aggregation. To further use GO–Austar for cancer PTT therapy, through the modification of reduced human serum albumin–folic acid conjugate (rHSA–FA) and loading IR780, the final probe GO–Austar@rHSA–FA@IR780 was prepared. The prepared probe showed excellent biocompatibility and superb phototoxicity towards MGC-803 cells *in vitro*. *In vivo*, the final probe dramatically increased tumor temperature up to 58.6 °C after 5 minutes of irradiation by an 808 nm laser, significantly inhibiting tumor growth and nearly eradicating subcutaneous tumors in mice. This research provides a novel and simple method for the synthesis of GO–Au nanocomposites, showcasing significant potential in biological applications.

Received 29th January 2024

Accepted 8th March 2024

DOI: 10.1039/d4ra00742e

[rsc.li/rsc-advances](https://rsc.li/rsc-advances)

## 1. Introduction

According to recent reports, there has been a rapid increase in cancer incidence and mortality rates worldwide.<sup>1</sup> Therefore, recognizing the growing challenges in cancer management, intensive efforts have been dedicated to seamlessly integrating cancer diagnosis and therapy.<sup>2–4</sup> This includes the incorporation of advanced techniques such as photothermal therapy (PTT), photodynamic therapy (PDT), and chemotherapy, reflecting a flexible approach to address the complexity of cancer treatment.<sup>5,6</sup> Compared with conventional treatments such as radiotherapy, chemotherapy, and clinical surgery, these innovative cancer treatment methods possess visualization and light-induced therapy efficacy. They effectively integrate

fluorescence imaging with *in vivo* therapy, providing a comprehensive approach to cancer treatment.<sup>7–9</sup>

PTT could generate thermal energy through the absorption of near-infrared (NIR) wavelength light (typically in the range of 700–900 nm). The excellent tissue penetration of NIR light ensures not only favorable therapeutic efficacy but also minimal side effects in the context of *in vivo* cancer cellular therapy.<sup>10,11</sup> To achieve the optimal therapeutic effect, photothermal reagents with high safety and excellent NIR absorption were chosen to construct nanoprobes for cancer diagnosis and therapy. Herein, the NIR dye IR780 iodide, characterized as a hydrophobic heptamethine indocyanine dye, has emerged as an excellent PTT reagent owing to its high stability, deep penetration, and favorable real-time imaging property, indicating that the photosensitive molecule IR780 could be used for cancer PDT, PTT therapy, as well as fluorescence imaging in cancer therapeutic applications.<sup>12,13</sup>

However, the limited hydrophilicity of IR780 hinders its clinical application. Biocompatible carriers are employed to overcome these challenges.<sup>14–16</sup> Plasmonic gold nanomaterials, including nanostars, nanorods, nanocages, and nanoprisms, exhibit substantial potential in bio-applications.<sup>17–19</sup> Particularly in cancer therapy, gold nanomaterials show favorable characteristics, such as low toxicity, excellent biocompatibility, chemical stability, and plasmon properties tunable in the NIR region.<sup>20,21</sup> Furthermore, the surface-resonant plasmon of nanoparticles is intricately linked to their size and morphology. To harness these properties, extensive efforts have been

<sup>a</sup>Institute of Nano Biomedicine and Engineering, Shanghai Engineering Research Center for Intelligent Instrument for Diagnosis and Therapy, School of Sensing Science and Engineering, Shanghai Jiao Tong University, Shanghai 200240, P. R. China. E-mail: zhangamin@sjtu.edu.cn; dx cui@sjtu.edu.cn

<sup>b</sup>Department of Food Science & Technology, School of Agriculture & Biology, Shanghai Jiao Tong University, Shanghai 200240, China

<sup>c</sup>Radiology Department of Ruijin Hospital, Shanghai Jiao Tong University School of Medicine, 197 Ruijin Second Road, Shanghai 200025, China

<sup>d</sup>Department of Orthopedics, The First Affiliated Hospital of Bengbu Medical College, Bengbu City, Anhui Province, P. R. China

† Electronic supplementary information (ESI) available. See DOI: <https://doi.org/10.1039/d4ra00742e>

‡ These authors contributed equally to this work.



dedicated to precisely regulate their surface-resonant plasmon in the NIR region for *in vivo* applications.<sup>22</sup> This involves the advancement of photothermal transducers for cancer therapy, which are capable of converting absorbed near-infrared (NIR) light into localized heat. These transducers facilitate directed photothermal therapy specifically targeting tumor tissue, ensuring minimal damage to normal biological tissues owing to their excellent tissue penetration. Moreover, the corresponding NIR absorption capability can be adjusted through the modification of the shape of the utilized gold nanomaterials. Star-shaped gold nanoparticles (Austar) have generated interest due to their simple synthesis method, distinctive plasmon band in the NIR window, and strong absorption in the NIR region.<sup>23</sup> Due to these intriguing properties, Austar has been widely applied in bio-imaging, nano-therapy, and nanomedicine.<sup>24,25</sup>

To diminish the aggregation of the prepared Austar, a common approach is to modify a surfactant layer to improve the hydrophilicity of the synthesized metal nanomaterials. However, numerous surfactants exhibit some biological toxicity.<sup>26–28</sup> To improve the biosafety of the obtained nanomaterials, minimizing the dosage of the traditional surfactant is highly desired.<sup>29</sup>

Recently, two-dimensional graphene and its derivatives, including graphene oxide and reduced graphene oxide, have attracted tremendous attention in the construction of biosensors and clinical applications.<sup>30–33</sup> The unique structure of graphene oxide endows its favorable physico-chemical properties, such as the  $\pi$ - $\pi$  adsorption capacity, large surface area, and abundant functional groups. Consequently, it has emerged as an excellent platform for constructing biosensors and serving as carriers for various inorganic nanomaterials and organic molecules.<sup>34,35</sup> Interestingly, some works mentioned that carbon nanomaterials including GO and carbon nanotubes could be used as reductants and surfactants to produce metal nanoparticles and semiconductor nanoparticles directly in the absence of conventional reductants and surfactants, which could effectively reduce the use of the toxic reductant and surfactant reagents.<sup>36</sup>

In this work, we synthesized gold nanostars on the surface of graphene oxide *in situ*, in which GO could be used as a reductant and surfactant in the formation process of Au nano seeds under UV-light irradiation without adding any other reductants and surfactants. Based on the GO–Au seeds, we directly prepared Au nanostars on the surface of GO. Through a systemic preparation process, we first synthesize gold seeds on the surface of GO *in situ* by a UV-induced method. Then, according to the commonly seed-mediated method, Austar supported on graphene oxide was synthesized based on the above-acquired GO–Au seeds (GO–Austar) with a near-infrared (NIR) absorption range overlapping with IR780. In this process, GO served multiple roles as a surfactant to protect Au seeds and Austar from aggregation, reductant to synthesize Au seeds, as well as a carrier to load IR780 molecules. To enhance the biocompatibility and targeted ability of probes, the composites (rHSA–FA)-combined reduced human serum albumin (rHSA) and FA were cross-linked onto the surface of Austar and GO *via* chemical bonding Au–S through  $\pi$ - $\pi$  stacking. After that, the NIR fluorescent molecule IR780 was loaded

to realize photothermal therapy (PTT) cooperating with Austar, which could be effectively released from the surface of GO at the tumor sites (details are displayed in Scheme 1). Such hybrid nanomaterials (GO–Austar@rHSA–FA@IR780) have been successfully prepared for gastric cancer PTT therapy, and exhibited favorable biocompatibility and excellent PTT therapeutic ability due to the synergistic NIR absorption of Austar and IR780. The demonstrated UV-induced strategy presented a promising approach for the design of low-toxicity nanomaterials in the context of cancer diagnosis and therapy.

## 2. Experimental details

### 2.1. Reagents and materials

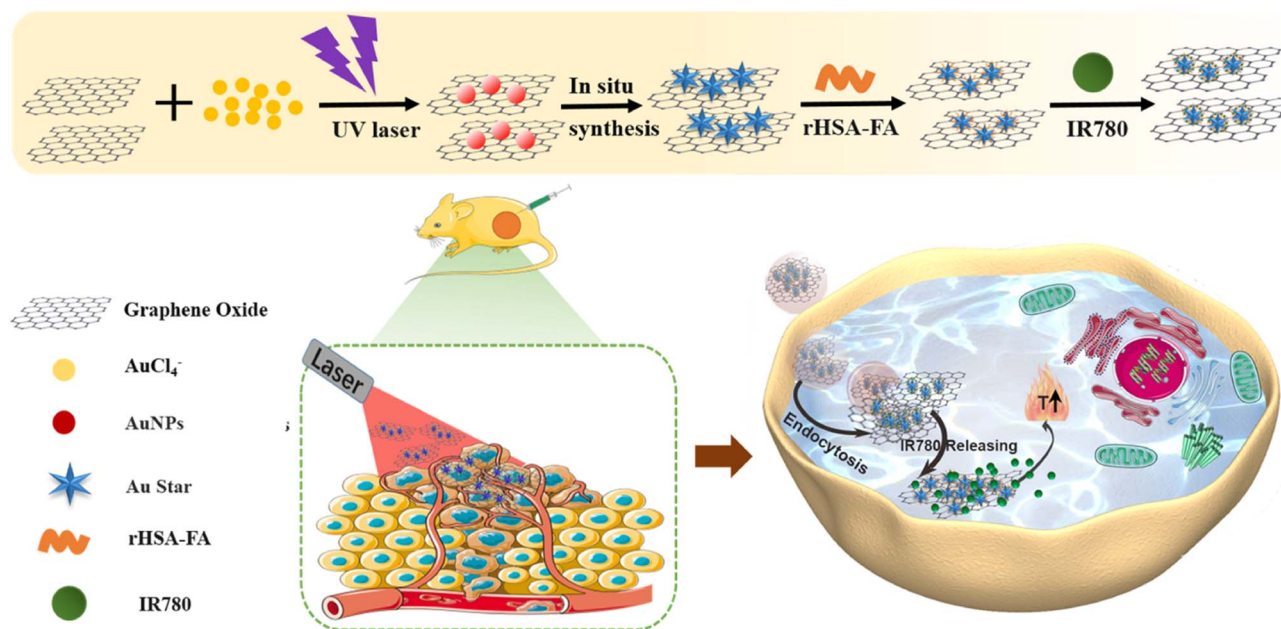
Gold chloride trihydrate ( $\text{HAuCl}_4 \cdot 3\text{H}_2\text{O}$ ) was bought from Shanghai Titan Polytron Technologies, Inc. (Shanghai, China). In addition, chemical reagents including hydrochloric acid (HCl, 37%), sulfuric acid ( $\text{H}_2\text{SO}_4$ , 98%), nitric acid ( $\text{HNO}_3$ ,  $\geq 97.2\%$ ), folic acid (FA), anhydrous dimethyl sulfoxide (DMSO), silver nitrate ( $\text{AgNO}_3$ ) and ascorbic acid (AA) were all obtained from Sinopharm Chemical Reagent Co., Ltd. (Shanghai, China). *N*-Hydroxysuccinimide (NHS) and *N*-(3-dimethylaminopropyl)-*N*-ethylcarbodiimide hydrochloride (EDC) were obtained from Aladdin Reagent Co., Ltd. (Shanghai, China). Annexin V-FITC/PI Apoptosis Detection Kit, 2-(4-amidinophenyl)-6-indolecarbamide dihydrochloride (DAPI), Cell Counting Kit (CCK-8) and Calcein-AM/PI Double Stain Kit were all bought from YEASEN Corporation (Shanghai, China). Fetal bovine serum (FBS), Dulbecco's Modified Eagle's Medium (DMEM), penicillin–streptomycin, and trypsin–EDTA used for cell culture were all obtained from Gibco Life Technologies. All chemical reagents used here were of analytical grade without further purification. The double-distilled water (18.2 M $\Omega$ , Millipore Co., USA) was employed in all experiments. In addition, phosphate-buffered solutions (PBS, 0.1 M) were acquired by using 0.1 M  $\text{Na}_2\text{HPO}_4$  and 0.1 M  $\text{KH}_2\text{PO}_4$ .

### 2.2. Characterization equipment

The morphology information of various nanomaterials was monitored by field emission transmission electron microscopy (FE-TEM, Talos F200X) and scanning electron microscopy (SEM, Zeiss Ultra5). The hydrodynamic sizes of various nanomaterials were investigated by dynamic light scattering (DLS, Nano Brook Omni Zeta/PLS, Brook, USA). The UV-vis spectrophotometer (Varian Inc., Palo Alto, CA, USA) was used to study the modified information of the probes. Fourier transform infrared spectroscopy (FTIR) of different nanomaterials was carried out on a Fourier transform infrared spectrometer (Nicolet 6700). The element binding energy was analyzed by X-ray photoelectron spectroscopy (AXIS Ultra DLD).

### 2.3. Synthesis of GO with small size

In this process, layered graphene oxide with large sizes was synthesized according to the previously reported Hummer's method.<sup>37</sup> To obtain graphene oxide with a small size, 500 mg of the above-acquired GO nanolayer was ultrasonicated in 40 mL of



Scheme 1 Schematic illustration of the preparation and therapeutic mechanism of GO–Austar@rHSA–FA@IR780.

an acid mixture containing strong sulfuric acid and concentrated nitric acid ( $v/v = 3/1$ ) for 7 h. Then, the obtained GO was centrifuged at 10 000 rpm for 20 min, followed by washing with HCl (4%) under sonication for three times to remove a large proportion of excess acid. After that, the acquired GO was repeatedly washed with deionized water until most of the GO could not be centrifuged. Then, the above-obtained GO was purified by dialysis in water for 5 days. Finally, the purified GO solution was filtrated by a 0.22  $\mu\text{m}$  filter membrane to remove large-size GO sheets and obtain GO with a size around 200 nm. Finally, the GO was lyophilized for further use.

#### 2.4. Synthesis of graphene oxide modified with gold seeds (GO–Au seeds)

In this process, 5 mg of purified GO powder with a small size was dissolved in 20 mL of pure water with ultrasonication to form a GO solution. Then, 66  $\mu\text{L}$  HAuCl<sub>4</sub> solution (242.81 mM) was mixed with GO solution under stirring. The pH of the mixture was regulated by 1 M sodium hydroxide solution to a pH value of 11. After adjusting, the brown solution was irradiated with UV light at an energy of 1000 J for 120 min. The acquired GO–Au solution was stored in the dark and acted as seeds for GO–Austar nanocomposite preparation.

To obtain the GO–Austar nanocomposites, the common seed-mediated method was utilized. In brief, 2 mL of the above-synthesized GO–Au seeds solution was diluted with 38 mL pure water with stirring. After that, 20.8  $\mu\text{L}$  HAuCl<sub>4</sub> solution (242.81 mM), 440  $\mu\text{L}$  HCl (1 M), and 2.2 mL AgNO<sub>3</sub> (3 mM) were successively added by stirring. Then, 1.6 mL AA (0.1 M) was added to the mixture and stirred for 1 min. Finally, the product GO–Austar was centrifuged at 8500 rpm for 5 min and redissolved in 1 mL PBS for further use.

#### 2.5. Preparation of rHSA–FA and crosslinking procedure of rHSA–FA onto GO–Austar

To enhance the biocompatibility of the final probes, we employed rHSA–FA composites, which consist of reduced human serum albumin (rHSA) and the targeted molecule folic acid (FA), to modify GO–Austar. In brief, 1 g FA powder was dissolved in 50 mL dimethyl sulfoxide (DMSO). Subsequently, 1.08 g 1-ethyl-3-(3-dimethylaminopropyl)carbodiimide hydrochloride (EDC·HCl) and 651 mg *N*-hydroxysuccinimide (NHS) were added to activate the FA in the dark for 12 h at room temperature. After repeated centrifugation and washing with a mixture of cold acetone and diethylether ( $v/v = 3/7$ ) to remove insoluble byproduct (dicyclohexylurea), the activated FA (FA–NHS) was lyophilized. Moreover, the reduced human serum albumin (rHSA) was prepared by adding 250  $\mu\text{L}$  NaBH<sub>4</sub> (1 M) into 10 mL HSA solution (4 mg mL<sup>-1</sup>). After 2 h stirring, 50 mg FA–NHS was added to the previously obtained rHSA solution for 6 h crosslinking. Ultimately, the excess FA–NHS was removed by centrifugal ultrafiltration (3 K MWCO), and the acquired rHSA–FA composites were lyophilized and stored at  $-20\text{ }^{\circ}\text{C}$ .

To attach rHSA–FA onto the surface of GO–Austar, 1 mg rHSA–FA was dissolved in 1 mL PBS, and then mixed with the previously obtained GO–Austar solution. After 6 h stirring, the products were centrifuged and washed with PBS three times. Finally, the nanocomposites GO–Austar@rHSA–FA were dissolved into 1 mL PBS, and stored in darkness.

#### 2.6. Loading IR780 onto GO–Austar@rHSA–FA

To enhance the PTT therapy, IR780 was loaded into the GO–Austar@rHSA–FA to construct the nanoprobes. In brief, the IR780 was firstly dissolved into DMSO with a concentration of 200 mg mL<sup>-1</sup>. Subsequently, 50  $\mu\text{L}$  IR780 solution was mixed

with GO–Austar@rHSA–FA (2 mg mL<sup>-1</sup>) with stirring for 8 h at 37 °C. Finally, the obtained nanocomposites GO–Austar@rHSA–FA@IR780 were washed three times with PBS to remove residual reagents by centrifugation (8000 rpm min<sup>-1</sup>, 3 min). Moreover, the collected supernatant solution was used to calculate the unloaded amount of IR780. Finally, the sequential nanocomposites GO–Austar@rHSA–FA@IR780 were redispersed in 1 mL PBS (pH 7.4) for further use.

The entrapment efficiency (EE) and loading rate (LR) of IR780 in GO–Austar@rHSA–FA@IR780 were calculated according to the following equations:

$$EE (\%) = \frac{\text{weight of IR780 loaded in nanocomposites}}{\text{weight of IR780 added initially}} \times 100\%$$

$$LR (\%) = \frac{\text{weight of IR780 in nanocomposites}}{\text{weight of IR780} + \text{weight of GO} - \text{Austar@rHSA} - \text{FA}} \times 100\%$$

## 2.7. Characterization of various materials

In this work, the field emission transmission electron microscope (FE-TEM, Talos F200X), atomic force microscope (AFM, Dimension Icon & FastScan Bio, USA), and Zetasizer Nano ZS were used to analyze the morphology information of various nanomaterials. Moreover, energy-dispersive X-ray spectroscopy (EDS) was employed to investigate the elemental distribution of nanomaterials, while X-ray photoelectron spectroscopy was utilized to analyze changes in elemental valence states. Furthermore, UV-vis spectrophotometry (Varian Inc., Palo Alto, CA, USA) was carried out to study the UV-vis absorbance spectra of nanomaterials.

## 2.8. Cell lines and culture conditions

The Dulbecco's modified Eagle medium (DMEM) containing 10% (v/v) fetal bovine serum, 100 U mL<sup>-1</sup> penicillin, and 0.1 mg mL<sup>-1</sup> streptomycin (named as cell medium) was used in this work to culture man gastric cancer (MGC-803) cells at 37 °C with 5% CO<sub>2</sub>. As the cells were in a logarithmic growth phase, they were applied to our experiment. Additionally, trypsin/EDTA was used to subculture MGC-803 cells.

## 2.9. Cytotoxicity of various materials

The cytotoxicity assay is crucial to studying the toxicity of constructed probes for further cancer therapy and assaying the therapeutic efficacy. In this work, Calcein-AM and PI Staining Technology, CCK-8 analysis, and apoptosis assay were applied to investigate the biosafety and phototoxicity of various materials, including free IR780, GO–Austar@rHSA–FA, and GO–Austar@rHSA–FA@IR780 nanoprobes.

**CCK-8 assay.** Briefly, MGC-803 cells were incubated in 96-cell plates (5 × 10<sup>3</sup> cells per well). After 24 h incubation, 100 μL fresh complete medium containing IR780, GO–Austar@rHSA–FA and GO–Austar@rHSA–FA@IR780 at various dosages were added into 96-cell plates, where the IR780 dosage ranged from 1 to 6 μg mL<sup>-1</sup> and GO–Austar@rHSA–FA were at 2–12 μg mL<sup>-1</sup>

(control group: blank, 100 μL fresh complete medium). After 12 h endocytosis, the cells were washed with PBS twice, and then incubated with 100 μL fresh complete medium. Following that, the cells were irradiated with an 808 nm laser (1.0 W cm<sup>-2</sup>, 5 min), and the cells were in the dark as comparisons. After that, the cell viability in various groups was analyzed by CCK-8 assay when incubated for 24 h in the dark. Moreover, a microplate reader with an absorbance peak at 450 nm was used to calculate the cell viability, and the obtained data were processed by the followed formula:

$$\text{Cell viability} = (\text{OD}_{\text{treated}} - \text{OD}_{\text{blank}}) / (\text{OD}_{\text{control}} - \text{OD}_{\text{blank}})$$

**Apoptosis assay.** The cell apoptosis was investigated on a BD FACS Calibur (BD Biosciences, Mountain View, CA) after the treated cells in various groups were stained by Annexin V-FITC/PI Apoptosis Detection Kit (Yeasen, Shanghai). Briefly, the MGC-803 cells in 6-cell plates (1 × 10<sup>5</sup> cells per well) were firstly interacted with PBS, IR780, GO–Austar@rHSA and GO–Austar@rHSA–FA@IR780 (IR780: 3 μg mL<sup>-1</sup>, GO–Austar@rHSA: 6 μg mL<sup>-1</sup>) for 12 h. After irradiation with or without 1.0 W cm<sup>-2</sup> 808 nm for 5 min and incubation for an additional 12 hours, the cells were collected and stained in 400 μL of binding buffer including 5 μL of Annexin V and 10 μL of PI for 10 min. Ultimately, the stained cells were investigated on flow cytometry, and the experimental data were analyzed by FlowJo 10.0 software.

**Calcein-AM and PI staining study.** To visualize the therapeutic efficacy of various materials, the MGC-803 cells were first treated according to the same steps as the cells in the CCK-8 assay after being incubated in 24-cell plates for 24 h (1.0 × 10<sup>4</sup> cells per well). In brief, the cells in 24-cell plates were first interacted with PBS, IR780, GO–Austar@rHSA–FA, and GO–Austar@rHSA–FA@IR780 (IR780: 3 μg mL<sup>-1</sup>, GO–Austar@rHSA–FA: 6 μg mL<sup>-1</sup>) for 12 h. Then, the treated cells were irradiated with or without a NIR laser (808 nm, 1 W cm<sup>-2</sup>) for 5 min. After an extra 12 h incubation, the cells were stained with calcein-AM (2.0 μM) and PI (1.5 μM), and finally observed by fluorescence microscope.

## 2.10. Animals and tumor model

The female nude mice at 6 weeks old and 18–22 g were purchased from Shanghai Jiesijie Laboratory Animal Co., Ltd. (China). All animal procedures were performed in accordance with the Guidelines for the Care and Use of Laboratory Animals of Shanghai Jiao Tong University, and approved by the Animal Ethics Committee of Animal Research's Ethical Requirements (approval number 202201012). To generate a gastric cancer tumor model, MGC-803 cells (2 × 10<sup>6</sup> in 100 μL PBS) were subcutaneously injected into the right flank of isoflurane-anesthetized mice. As the tumor size increased to 100 mm<sup>3</sup>, the mice were used for animal experiments.

## 2.11. *In vivo* therapy effect of mice tumor

To investigate the *in vivo* therapy effect on mice tumors during various materials, the MGC-803 tumor-bearing mice were firstly

subcutaneously injected separately with 100  $\mu\text{L}$  PBS (used as control), free IR780, GO-Austar@rHSA-FA and GO-Austar@rHSA-FA@IR780 (IR780: 5 mg  $\text{kg}^{-1}$ , GO-Austar@rHSA-FA: 25 mg  $\text{kg}^{-1}$ ).

After 24 h post-injection, the tumor sites were treated with 1.0  $\text{W cm}^{-2}$  808 nm laser radiation for 5 min. Meanwhile, the temperature changes at the tumor sites and the infrared pictures were recorded by utilizing an infrared camera. Afterward, the relative tumor volume and mice weight were measured every 3 days within 18 days, and the changes in tumor sites from each group were recorded every day by a camera.

### 2.12. Statistical analysis

All data in this work were shown as means  $\pm$  SD.

## 3. Results and discussion

### 3.1. Preparation and characterization of various materials

The size and morphology of the GO nanosheet were investigated by AFM (Fig. 1A). As shown in Fig. S2A,† the GO was shown to be almost single-layer sheets with an average width and length of 250 nm and 170 nm, respectively. The as-synthesized GO nanosheets were utilized as carriers to modify gold seeds. Subsequently, the GO-Austar was obtained by the gold seeds-mediated method, and its morphology was investigated by TEM. It can be observed that considerable Au nanoparticles with spherical or ellipse shape (average diameter: 12 nm) are deposited on the thin slice GO nanostructure (Fig. 1B and S2B†). The AFM topography image of GO-Au seeds in Fig. S1† also confirmed that Au seeds were stacked on the surface of GO. Normal Au seed synthesis methods need strong reductants like  $\text{NaBH}_4$  (ref. 38) or other violent atmospheres to trigger the occurrence of a reduction reaction. The UV-assisted synthesis method could induce the photoreduction reaction with a mild atmosphere, showing excellent safety and feasibility.

The final nanocomposites of GO-Austar@rHSA-FA were obtained by the crosslinking procedure of rHSA-FA towards the GO-Austar nanosheet. The TEM in Fig. 1C shows the successful preparation of GO-Austar@rHSA-FA, and the HSA-FA decoration also enhanced the contrast of nanocomposites. As shown in Fig. S2C,† the morphology of Austar exhibited outstanding size uniformity. The average diameter of Austar and GO-Austar@rHSA-FA was  $45.67 \pm 3.93$  nm and  $270.8 \pm 37.2$  nm, respectively, analyzed by image J. The high magnification TEM image of GO-Austar@rHSA-FA showed that numerous spikes stretched from their surfaces (Fig. 1D). The hydrodynamic particle sizes of GO-Au seeds and GO-Austar@rHSA-FA were detected by DLS, and showed a uniform size distribution (Fig. S3†). However, the hydrodynamic diameter of GO-Austar@rHSA-FA was 357.7 nm, which is much larger than the TEM diameter and could not reflect the real particle size. Results of GO-Austar@rHSA-FA were further confirmed by the EDX energy spectrum (Fig. 1E). The EDX energy spectrum also revealed major elemental proportion in GO-Austar@rHSA-FA, indicating atomic percentages of 45.27%, 13.67%, and 41.06% for C, O, and Au, respectively. The synthesis of conventional

gold nanostars requires CTAB,<sup>39</sup> Triton X,<sup>40</sup> and other surfactants to control the particle size and prevent their aggregation. The employment of GO enabled the surfactant-free synthesis of gold nanostars, obviously reducing the preparation difficulty of Au nanoparticles.

To investigate the mechanism in the formation of GO-Austar, we conducted X-ray photoelectron spectroscopy (XPS) analyses on both GO and GO-Au nanocomposites. The full spectra in Fig. S4† unveil the extensive Au production on the surface of GO. Referring to the typical XPS spectrum of the carbon element, the C 1s binding energy spectrum was deconvoluted into three distinct peaks, including 284.76 eV (C-C in aromatic rings), 286.45 eV (C-O), and 287.98 eV (O-C=O). As depicted in Fig. 2A and B, the signals at 287.98 eV (O-C=O) increased noticeably after the production of Austar. This evidence indicates that GO serves as a reducing agent, facilitating the reduction of  $\text{Au}^{3+}$  in the presence of UV radiation. Benefiting from the robust UV absorption capability of GO, the absorbed UV energy triggers the photoreduction reaction of  $\text{Au}^{3+}$ , thereby promoting the generation of the Au nanocomplex. The Au 4f binding energy spectra in Fig. 2C and D also verified the production of Au nanoparticles.

UV-vis spectroscopy was used to testify to the systematic immobilization of the final probes. The change of absorption of GO-Au seeds under different pH and different times were recorded in Fig. 3A and B. The UV-vis absorbance spectra of the GO-Au seed (Fig. 3C curve b) showed the absorption peaks at 345 nm and 535 nm, revealing the formation of the GO-Au seed. The longitudinal SPR absorption of GO-Au seed red-shifted to 816 nm after the Au-seed was self-grown to Au-star onto the GO sheet (Fig. 3C curve c). The result is consistent with the morphological changes observed in the TEM image. As shown in Fig. 3D, GO-Austar (curve a) exhibited a typical absorption peak at 245 nm, corresponding to the  $\pi$ - $\pi^*$  transition of aromatic areas in the synthesized GO-Austar. Furthermore, the composites rHSA-FA (curve b) displayed two distinct peaks at 280 nm and 346 nm as a consequence of the absorption of rHSA and FA correspondingly. Compared with the bare GO-Austar (curve a), there was an extra peak at 348 nm (curve c) due to the presence of FA and a distinct red-shifted peak at 260 nm because of the superposition of GO-Austar and rHSA. Furthermore, because of the characteristic absorption peak at 776 nm of IR780 (curve d), a broad and obvious absorption peak emerged across from 600 nm to 900 nm after loading the IR780 in GO-Austar (curve e), indicating the successful integration of IR780 and GO-Austar, as well as the favorable stability of the loaded IR780.

### 3.2. Cellular uptake and intracellular distribution

The distribution of various materials of free IR780 and GO-Austar@rHSA-FA@IR780 in MGC-803 were investigated *via* confocal laser scanning microscopy (CLSM) and flow cytometry (FC) (Fig. 4A and B). As shown in Fig. 4A, only dim red fluorescence was monitored in the cells treated with free IR780 for 4 h, indicating the low amount of IR780 that entered the cells. On the contrary, owing to the FA receptor

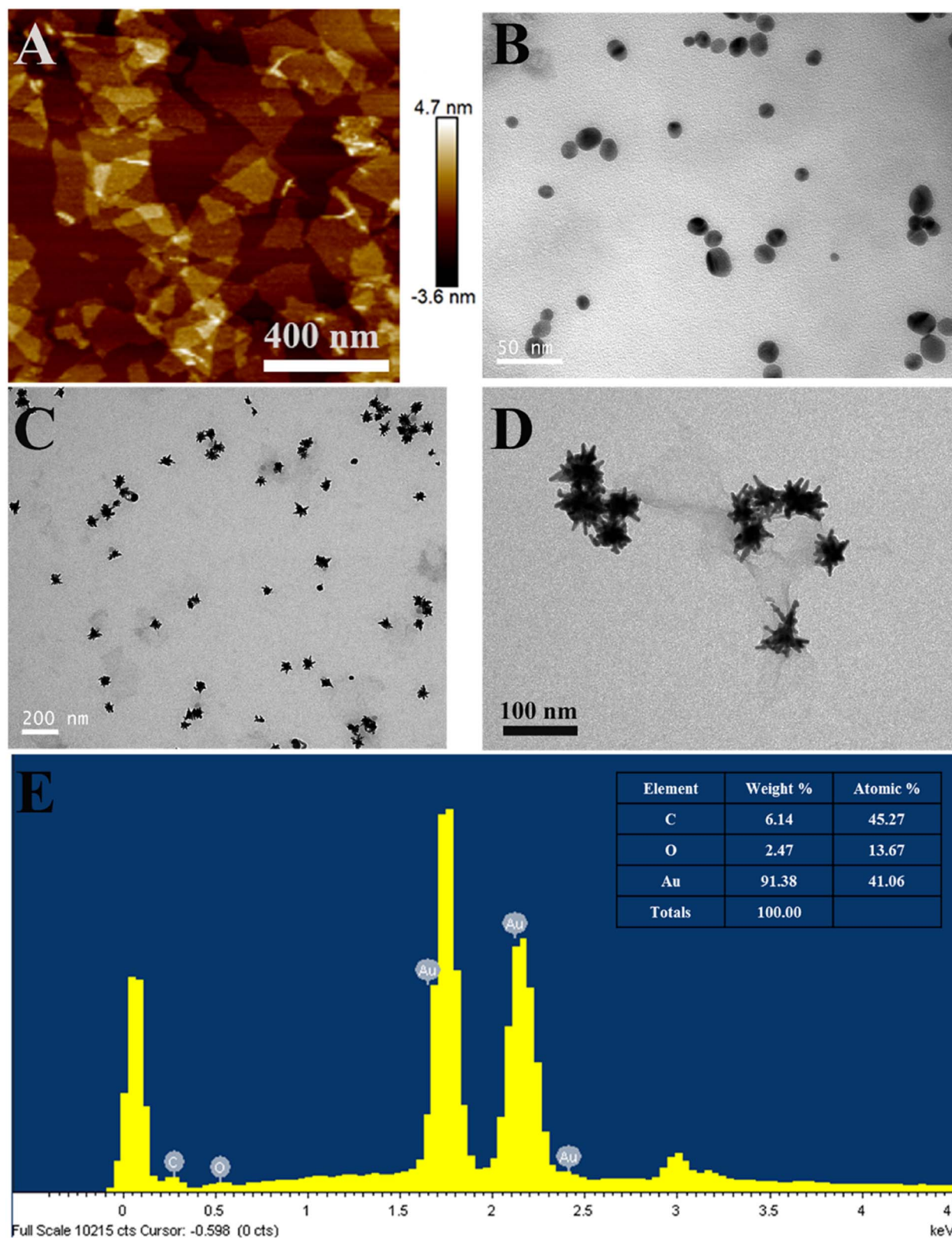


Fig. 1 Synthesis and characterization of GO-Austar@rHSA-FA. (A) AFM topography image of GO. TEM image of GO-Au seeds (B) and (C) GO-Austar@rHSA-FA. (D) Highly-magnified TEM image of GO-Austar@rHSA-FA. (E) EDX energy spectrum of GO-Austar@rHSA-FA.

targeting ability of GO-Austar@rHSA-FA@IR780, bright fluorescence was detected in the cytoplasm after the MGC-803 cells were co-incubated with GO-Austar@rHSA-

FA@IR780 for 4 h. Meanwhile, the mean fluorescence values examined by FCM also verified the higher fluorescence intensity of the MGC-803 cells after incubation with the GO-

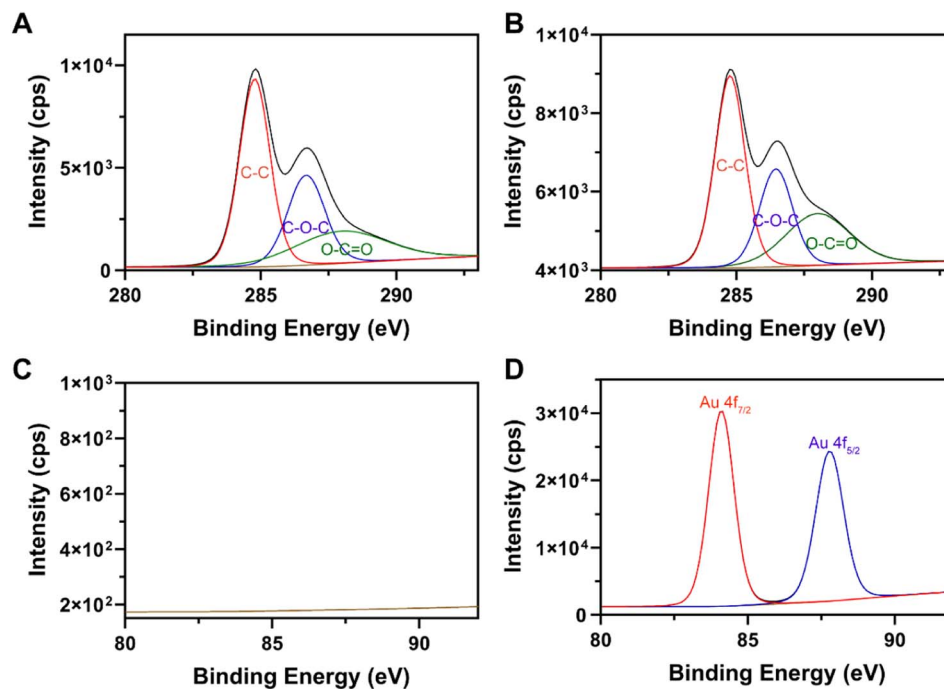


Fig. 2 The high-resolution XPS spectra of GO and GO–Austar. C 1s XPS spectra of (A) GO and (B) GO–Austar. Au 4f XPS spectra of (C) GO and (D) GO–Austar.

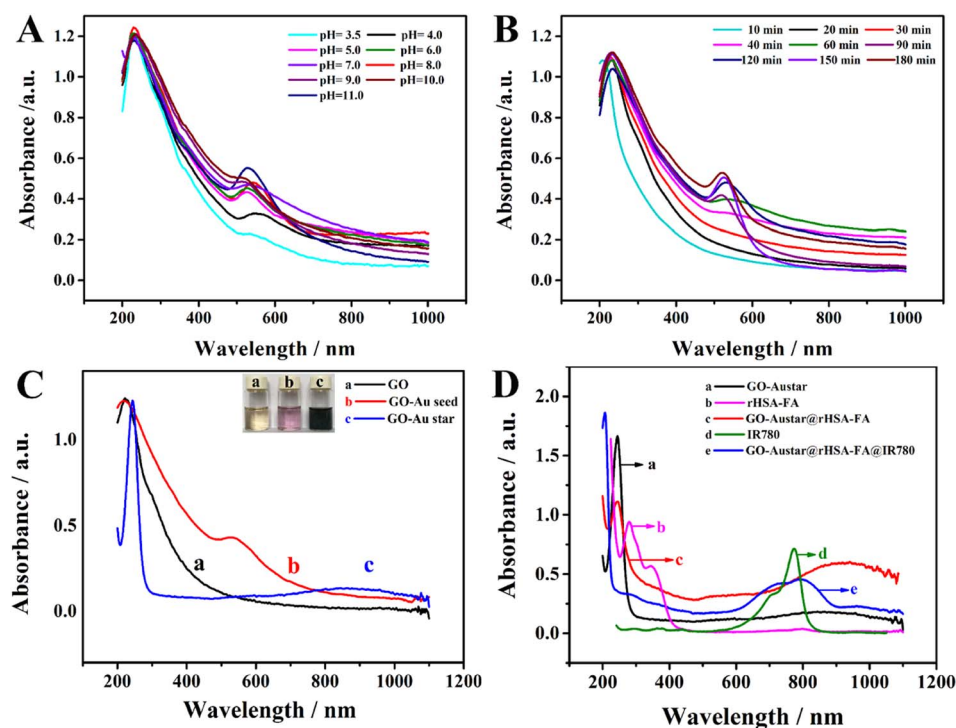
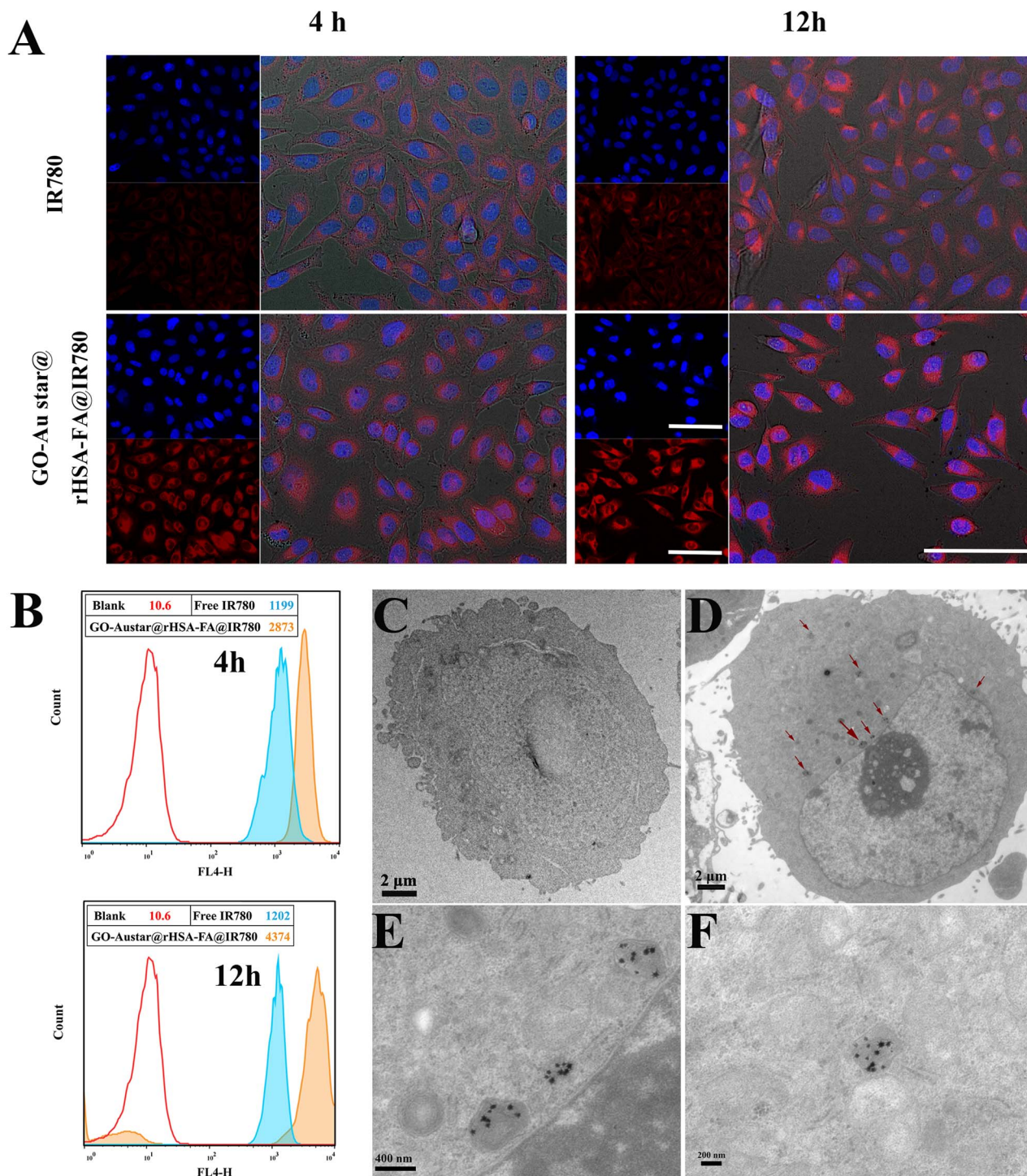


Fig. 3 UV-vis absorbance spectra of the prepared nanomaterials. GO–Au seeds were measured under different pH (A) at different times (B). (C) UV-vis absorbance spectra of GO (a), GO–Au seeds (b), GO–Austar (c). The inserted photographs are GO, GO–Au seeds, and GO–Austar, respectively, dispersed in water. (D) UV-vis absorbance spectra of GO–Austar (a), rHSA–FA (b), GO–Austar@rHSA–FA (c), IR780 (d), and GO–Austar@rHSA–FA@IR780 (e).

Austar@rHSA–FA@IR780, which was 2.4-fold higher than that of the MGC-803 treated with IR780 (Fig. 4B). The red fluorescence intensity gradually increased over time, and the

most significant difference in the quantity of cellular uptake between GO–Austar@rHSA–FA@IR780 and free IR780 occurred after 12 h of incubation with a 3.6-fold higher mean



**Fig. 4** *In vitro* cellular uptake of GO–Austar@rHSA–FA@IR780 by MGC-803. (A) Confocal images, scale bar: 2 μm. (B) Flow cytometry analysis of MGC-803 cells exposed to free IR780 and GO–Austar@rHSA–FA@IR780 for 4 h and 12 h. Red, blue, and yellow histograms represent the cellular uptake of PBS, free IR780, and GO–Austar@rHSA–FA@IR780, respectively. (C) Representative TEM images of MGC-803. (D–F) Ultrastructure of MGC-803 cells after 24 h incubation with GO–Austar@rHSA–FA@IR780; red arrows indicate the GO–Austar@rHSA–FA@IR780 located in the lysosome.

fluorescence intensity *via* FCM. All results indicated that FA ligands on the surface of the GO–Austar@rHSA–FA@IR780 nanoprobe could enhance the targeting effectiveness toward gastric cancer MGC-803 cells. The fabricated GO–

Austar@rHSA–FA@IR780 might provide an alternative superior approach for transporting abundant IR780 into the MGC-803 cells. Furthermore, the internalization of the nanoprobe was intuitively examined by TEM (as shown in



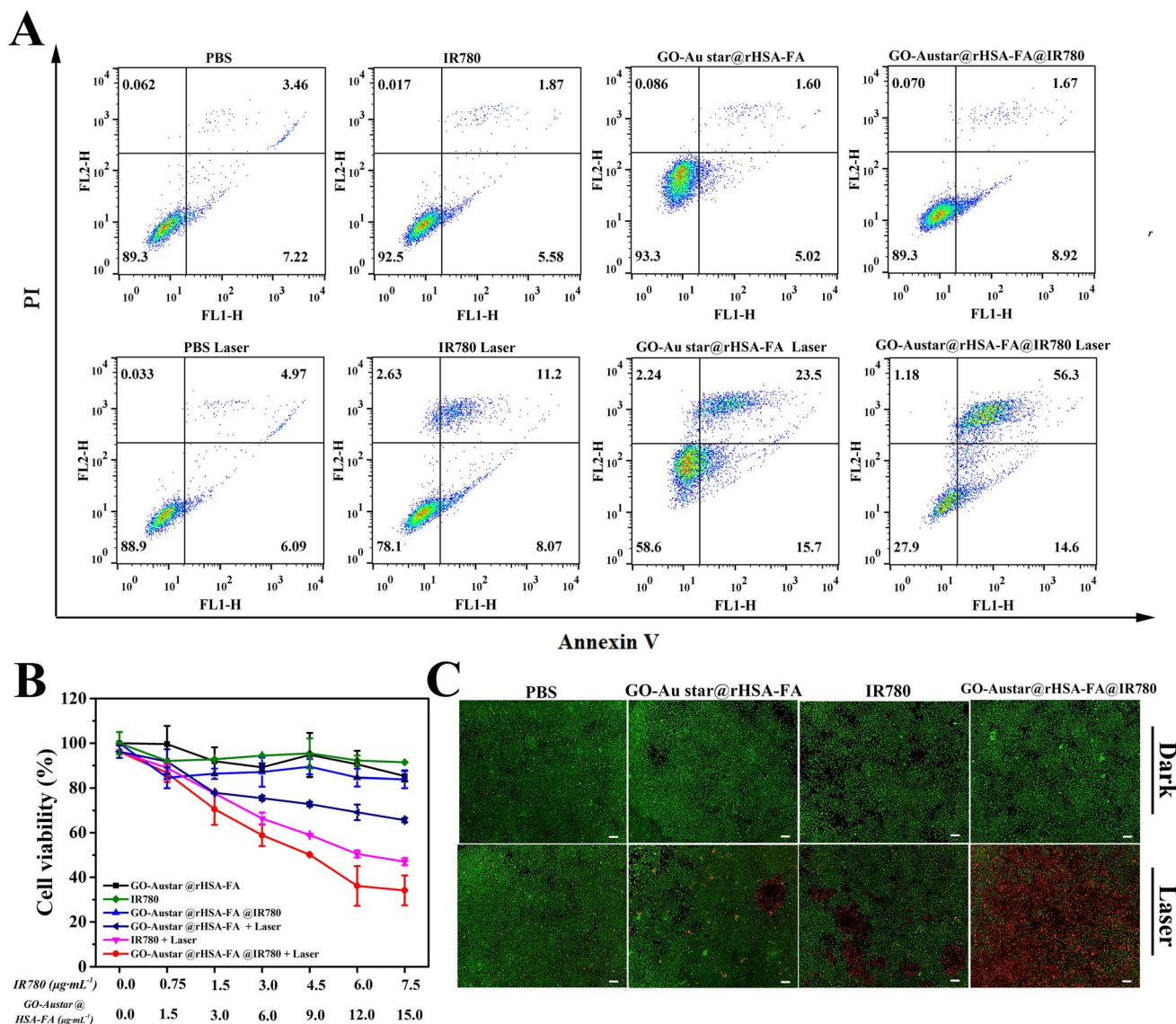


Fig. 5 *In vitro* cellular toxicity. (A) MGC-803 cell death induced by PTT/PDT of PBS, free IR780 and GO-Austar@rHSA-FA, GO-Austar@rHSA-FA@IR780 analyzed by flow cytometry, respectively. (B) Cell viability of MGC-803 cells after incubation with various concentrations of GO-Austar@rHSA-FA, free IR780, and GO-Austar@rHSA-FA@IR780 measured by CCK-8 assay. (C) Phototoxicity of MGC-803 cells conducted with PBS, free IR780 and GO-Austar@rHSA-FA, GO-Austar@rHSA-FA@IR780 with or without laser irradiation (NIR laser: 808 nm, 1 W cm<sup>2</sup>), respectively. (Scale bar, 100 μm).

Fig. 4C–F, denoted by red arrows). As shown in Fig. 4E, GO-Austar@rHSA-FA@IR780 were positioned in lysosomes and endosomes in aggregated style, and no nanoprobe were detected in the nucleus. We speculated that GO-Austar@rHSA-FA@IR780 was specifically recognized and endocytosed by the surrounding MGC-803 cells (over-expression of FA receptor).

### 3.3. *In vitro* cell toxicity

Good biocompatibility and superior phototoxicity were the prerequisites for a nano-platform based PDT/PTT to kill MGC-803. The cellular proliferation inhibition by free IR780, GO-Austar@rHSA-FA, and GO-Austar@rHSA-FA@IR780 was measured by CCK-8 assay. There was an obvious difference

between the NIR irradiation group and the dark group. The groups including free IR780, GO-Austar@rHSA-FA and GO-Austar@rHSA-FA@IR780 (IR780: 0–6 μg mL<sup>-1</sup>, GO-Austar@rHSA-FA: 0–12 μg mL<sup>-1</sup>) exhibited favorable biocompatibility without NIR irradiation, while the groups with NIR irradiation showed concentration-dependent photo-toxicity to gastric cancer cells. As shown in Fig. 5B, there was no obvious decline in the cell viability after treatment of PBS with or without NIR irradiation, which revealed that the laser power intensity remained within the safe range. Furthermore, the biocompatibility and photo-toxicity of various treatments (free IR780, GO-Austar@rHSA-FA, and GO-Austar@rHSA-FA@IR780) towards MGC-803 with or without laser irradiation (IR780: 3 μg mL<sup>-1</sup>, GO-Austar@rHSA-FA: 6 μg mL<sup>-1</sup>) were also

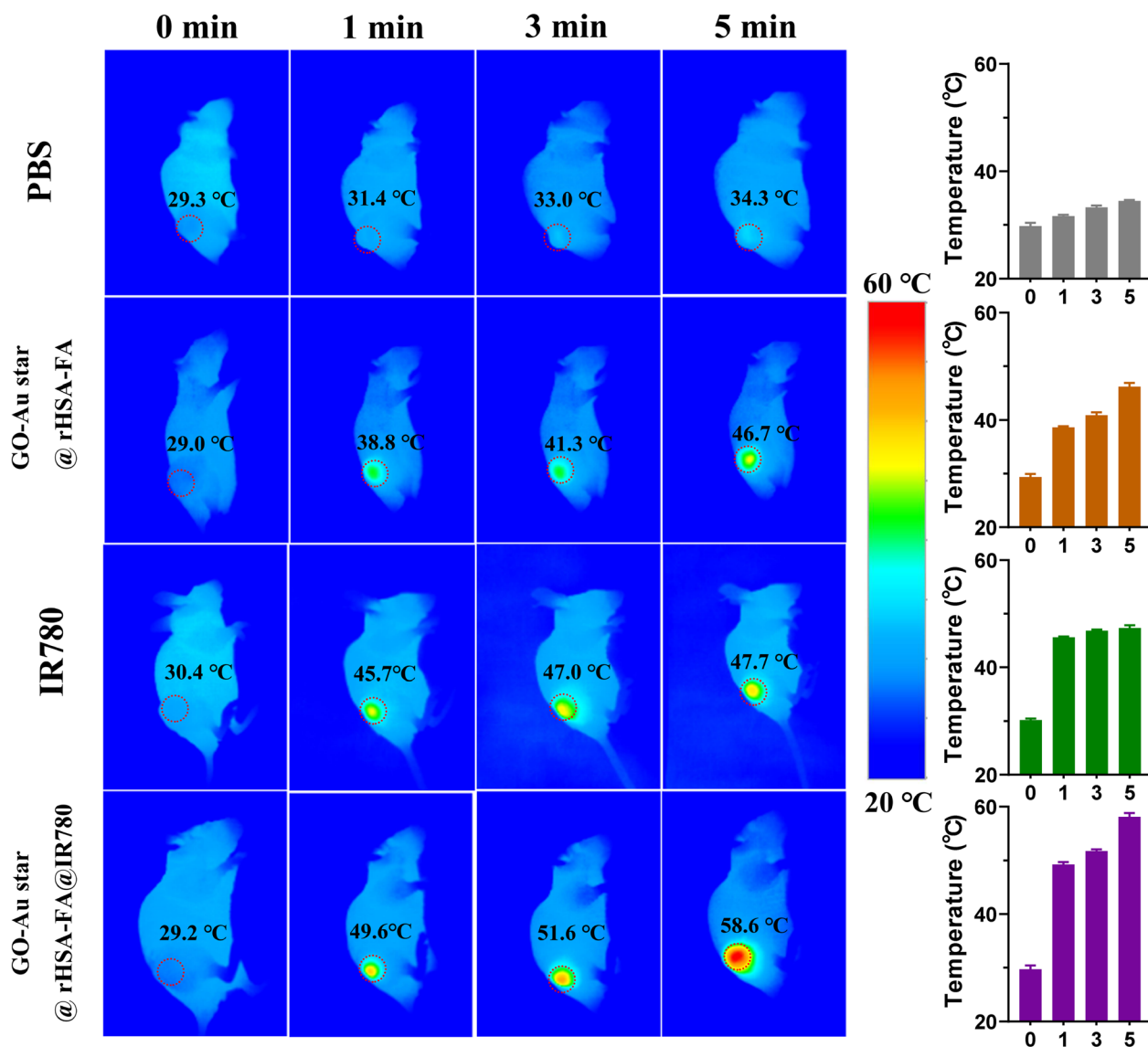


Fig. 6 Representative infrared thermography image of mice bearing MGC-803 upon irradiation ( $1.0 \text{ W cm}^{-2}$ , 808 nm, 5 min) after treatment with PBS, GO-Austar@rHSA-FA, free IR-780 and GO-Austar@rHSA-FA@IR780 ( $1 \text{ mg kg}^{-1}$  of IR780,  $5 \text{ mg kg}^{-1}$  of GO-Austar@rHSA-FA) to investigate the temperature variation in the tumor site over time (0 min, 1 min, 3 min, and 5 min).

confirmed by flow cytometry assay. Particularly, the total apoptosis ratio of MGC 803 cells treated with GO-Austar@rHSA-FA@IR780 was 70.9%, which is 3.6-fold higher than that with free IR780 (19.27%) and 1.8-fold with GO-Austar@rHSA-FA (39.2%) (as shown in Fig. 5A). Intuitively, the Annexin V-FITC and propidium iodide (PI) dual labeling assay was further used to detect stain dead and live cells to reconfirm the observation in the CCK-8 and flow cytometry assays. As shown in Fig. 5C, there were no obvious dead cells existing in the dark groups, signifying the good biocompatibility of the free IR780, GO-Austar@rHSA-FA, and GO-Austar@rHSA-FA@IR780. Furthermore, compared with the faint red fluorescence in the free IR780 and GO-Austar@rHSA-FA@IR780 groups with NIR irradiation, a strong red fluorescence was observed in the GO-Austar@rHSA-FA@IR780 nanoprobe

group, revealing that the nanoprobe has superior therapeutic efficacy as a result of the high loading efficiency of IR780 and GO-Austar, as well as good targeting capacity of FA. All the above results might be attributed to the superior synergistic PTT effect of IR780 and PDT effect of the GO-Austar of the nanoprobe, and the favorable specifically targeted effect of GO-Austar@rHSA-FA.

#### 3.4. *In vivo* therapeutic effect of GO-Austar@rHSA-FA in tumor-bearing mice

To evaluate the therapeutic effect of the GO-Austar@rHSA-FA@IR780 nanoprobe *in vivo*, PBS, GO-Austar@rHSA-FA, free IR 780 and GO-Austar@ rHSA-FA@IR780 ( $1 \text{ mg kg}^{-1}$  IR780) were intratumorally injected in MGC-803 tumor-bearing mice, and an 808 nm laser ( $1.0 \text{ W cm}^{-2}$ ) was used to irradiate the

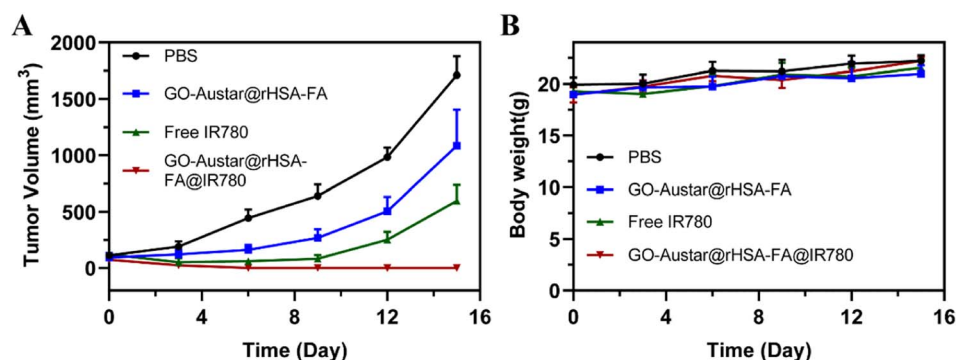


Fig. 7 *In vivo* photothermal therapy. (A) Tumor volume and (B) body weight changes of GO–Austar@rHSA–FA@IR780 after irradiation. MGC-803-bearing mice were treated with PBS, GO–Austar@rHSA–FA, free IR780 and GO–Austar@rHSA–FA@IR780. After 24 h, the tumor tissues were irradiated ( $1.0 \text{ W cm}^{-2}$ , 5 min).

tumor site of mice for 5 minutes after the injection of 24 hours. The temperature changes of the tumor site in different treatment groups were then monitored in real-time. As shown in Fig. 6, as the laser irradiation time increased, the temperature of the tumor site showed an escalating trend. The temperature of the tumor site in mice treated with free IR780 could reach  $47.7 \text{ }^\circ\text{C}$ , while the temperature of the tumor site in mice treated with the nanoprobe increased to  $58.6 \text{ }^\circ\text{C}$  under the same laser irradiation time. However, as a control, the temperature of the tumor site in mice treated with PBS could only rise to  $34.3 \text{ }^\circ\text{C}$ , which was not enough to cause thermal damage to the tumor, indicating that the intensity of the laser irradiation was safe. As shown in Fig. 7, within 18 days after laser irradiation, PBS-treated mice still had a relatively fast tumor growth rate. In addition, although IR780 has excellent PTT results, the IR780 group showed a lower tumor suppressive effect, which may be due to the hydrophobicity of IR780, which cannot effectively diffuse in tumor tissues. It is worth noting that the GO–Austar@rHSA–FA@IR780 group showed a good tumor growth inhibitory effect, and demonstrated its excellent PTT function. Furthermore, we also monitored the growth trend of tumors through cameras and recorded the changes in the tumor size in different treatment groups, as shown in Fig. S7.† Over time, the tumors still grew significantly in the different treatment groups without laser irradiation and the laser-irradiated PBS treated group. However, the tumor size of mice treated with GO–Austar@rHSA–FA@IR780 showed a significant reduction trend under laser irradiation, and the tumor site showed obvious scars after 3 days. After 15 days, the tumor tissue of the tumor-bearing mice was almost ablated after treatment with GO–Austar@rHSA–FA@IR780, and new normal tissue appeared at the tumor site. Remarkably, the tumor sites of GO–Austar@rHSA–FA@IR780 treated mice did not grow new tumor tissue after 30 days. However, although some tumors in the IR780 group were ablated, new tumor tissues still appeared within 15 days. This observation suggests that the inherent retention of the GO–Austar@rHSA–FA@IR780 nanoparticles leads to a substantial accumulation of nanoprobes at the tumor site, thereby enhancing its therapeutic effectiveness.

## 4. Conclusion

In this study, we leverage the strong absorption property of graphene oxide specifically in the ultraviolet (UV) wavelength range to trigger the photoreduction of  $\text{Au}^{3+}$ . Simultaneously, the abundance of functional groups on the surface of synthesized small graphene oxide provides ample growth sites for Au nanoparticles, significantly enhancing their *in situ* growth possibility on the graphene oxide surface. Additionally, modification of the HSA–FA conjugate enhanced the biocompatibility of GO–Austar. The *in situ* growth of GO–Austar on the graphene oxide surface was confirmed through AFM and TEM. EDX further revealed the elemental composition of GO–Austar@rHSA–FA; XPS indicated that GO serves as a reducer, facilitating the reduction of  $\text{Au}^{3+}$  in the presence of UV radiation. Upon loading with IR780, the photothermal effect of GO–Austar@rHSA–FA@IR780 was markedly enhanced, inducing significant apoptosis in MGC-803 cells *in vitro*. The *in vivo* heating experiment in mice revealed a rapid temperature increase at the tumor site under 808 nm laser irradiation, reaching  $58.6 \text{ }^\circ\text{C}$  within 5 minutes. Tumor therapeutic experiments also demonstrated that GO–Austar@rHSA–FA@IR780 significantly inhibits tumor growth, nearly eradicating subcutaneous tumors in mice. The novel preparation method of these gold nanostars provides a low-energy, environmentally friendly synthesis strategy, thereby accelerating the pace of their integration into biological applications.

## Data availability

Most of the data used in this study are presented in the article.

## Author contributions

Ang Gao: conceptualization, methodology, formal analysis, investigation, data curation, writing – original draft. Lijia Pei: methodology, formal analysis, investigation, data curation. Yunsheng Chen: formal analysis, investigation. Guan Liu: formal analysis, investigation. Amin Zhang: formal analysis, conceptualization. Daxiang Cui: conceptualization, formal

analysis, investigation, methodology, formal analysis, review, supervision.

## Conflicts of interest

The authors declare that there are no conflicts of interest regarding this article.

## Acknowledgements

This work was financially supported by Projects of International Cooperation and Exchanges NSFC (No. 82020108017), Innovation Group Project of National Natural Science Foundation of China (No. 81921002), National Key Research and Development Program of China (No. 2017FYA0205301), National Natural Science Foundation of China (No. 82102328 and 82272821), Projects of Shanghai Science and Technology Commission (No. 21DZ2203200 and 20142201300), and Natural Science Foundation of Shanghai (No. 22ZR1467600). They also are grateful for the financial support of the China Postdoctoral Science Foundation (No. 2020TQ0191 and 2021M702139).

## References

- 1 R. L. Siegel, K. D. Miller, N. S. Wagle and A. Jemal, *Ca-Cancer J. Clin.*, 2023, **73**, 17–48.
- 2 P. Liu, X. Shi, S. Zhong, Y. Peng, Y. Qi, J. Ding and W. Zhou, *Biomater. Sci.*, 2021, **9**, 2825–2849.
- 3 Z. Pei, H. Lei and L. Cheng, *Chem. Soc. Rev.*, 2023, **52**, 2031–2081.
- 4 P. L. Pranav, M. Jaggi, S. C. Chauhan and M. M. Yallapu, *J. Adv. Res.*, 2023, **51**, 197–217.
- 5 B. Feng, F. Zhou, B. Hou, D. Wang, T. Wang, Y. Fu, Y. Ma, H. Yu and Y. Li, *Adv. Mater.*, 2018, **30**, e1803001.
- 6 D. Wang, T. Wang, H. Yu, B. Feng, L. Zhou, F. Zhou, B. Hou, H. Zhang, M. Luo and Y. Li, *Sci. Immunol.*, 2019, **4**, eaau6584.
- 7 Y. Cai, X. Chen, J. Si, X. Mou and X. Dong, *Small*, 2021, **17**, e2103072.
- 8 X. S. Chen, J. J. Moon and J. Cheon, *Acc. Chem. Res.*, 2020, **53**, 2763–2764.
- 9 X. Li, W. Li, M. Wang and Z. Liao, *J. Control. Release*, 2021, **335**, 437–448.
- 10 X. Cui, Q. Ruan, X. Zhuo, X. Xia, J. Hu, R. Fu, Y. Li, J. Wang and H. Xu, *Chem. Rev.*, 2023, **123**, 6891–6952.
- 11 M. Overchuk, R. A. Weersink, B. C. Wilson and G. Zheng, *ACS Nano*, 2023, **17**, 7979–8003.
- 12 L. Wang and C. Niu, *J. Mater. Chem. B*, 2021, **9**, 4079–4097.
- 13 Y. Xue, K. Chen, Y. Chen, Y. Liu, J. Tang, X. Zhang and J. Liu, *ACS Nano*, 2023, **17**, 22553–22570.
- 14 W. Guo, Z. Li, H. Huang, Z. Xu, Z. Chen, G. Shen, Z. Li, Y. Ren, G. Li and Y. Hu, *ACS Appl. Mater. Interfaces*, 2022, **14**, 17008–17021.
- 15 Z. Li, Z. Chu, J. Yang, H. Qian, J. Xu, B. Chen, T. Tian, H. Chen, Y. Xu and F. Wang, *ACS Nano*, 2022, **16**, 15471–15483.
- 16 S. Wang, Z. Liu, Y. Tong, Y. Zhai, X. Zhao, X. Yue, Y. Qiao, Y. Liu, Y. Yin, R. Xi, W. Zhao and M. Meng, *J. Control Release*, 2021, **330**, 483–492.
- 17 R. Fu and Y. Xianyu, *Small*, 2023, **19**, e2300057.
- 18 A. Guinart, H. L. Perry, J. Wilton-Ely and T. D. Tetley, *Emerging Top. Life Sci.*, 2020, **4**, 627–643.
- 19 X. Zhao, H. Tang and X. Jiang, *ACS Nano*, 2022, **16**, 10066–10087.
- 20 M. Fan, Y. Han, S. Gao, H. Yan, L. Cao, Z. Li, X. J. Liang and J. Zhang, *Theranostics*, 2020, **10**, 4944–4957.
- 21 P. Kesharwani, R. Ma, L. Sang, M. Fatima, A. Sheikh, M. A. S. Abourehab, N. Gupta, Z. S. Chen and Y. Zhou, *Mol. Cancer*, 2023, **22**, 98.
- 22 A. Zhang, A. Gao, C. Zhou, C. Xue, Q. Zhang, J. M. Fuente and D. Cui, *Adv. Mater.*, 2023, **35**, e2303722.
- 23 C. L. Nehl, H. Liao and J. H. Hafner, *Nano Lett.*, 2006, **6**, 683–688.
- 24 Y. Liu, B. M. Crawford and T. Vo-Dinh, *Immunotherapy*, 2018, **10**, 1175–1188.
- 25 S. M. Mousavi, M. Zarei, S. A. Hashemi, S. Ramakrishna, W. H. Chiang, C. W. Lai and A. Gholami, *Drug Metab. Rev.*, 2020, **52**, 299–318.
- 26 G. Jena, K. Dutta and A. Daverey, *Chemosphere*, 2023, **341**, 140082.
- 27 O. S. Sutormin, E. M. Kolosova, I. G. Torgashina, V. A. Kratasyuk, N. S. Kudryasheva, J. S. Kinstler and D. I. Stom, *Int. J. Mol. Sci.*, 2022, **24**, 515.
- 28 A. R. Tehrani-Bagha, K. Holmberg, C. G. van Ginkel and M. Kean, *J. Colloid Interface Sci.*, 2015, **449**, 72–79.
- 29 I. Hering, E. Eilebrecht, M. J. Parnham, N. Günday-Türel, A. E. Türel, M. Weiler, C. Schäfers, M. Fenske and M. G. Wacker, *Environ. Toxicol. Pharmacol.*, 2020, **76**, 103353.
- 30 S. F. Tan, K. Reidy, S. Lee, J. Klein, N. M. Schneider, H. Y. Lee and F. M. Ross, *Adv. Funct. Mater.*, 2021, **31**, 2104628.
- 31 Z. W. Yang, C. W. Xu, H. H. Yan, Y. W. Liu, C. Yue, L. Y. Zhang, M. Shui, F. Hu and J. Shu, *Adv. Funct. Mater.*, 2021, **31**, 2103893.
- 32 L. Cao, Q. Liu, J. Ren, W. Chen, Y. Pei, D. L. Kaplan and S. Ling, *Adv. Mater.*, 2021, **33**, 2102500.
- 33 A. Gao, Y. Chen, H. Liang, X. Cui, A. Zhang and D. Cui, *Theranostics*, 2023, **13**, 4821–4835.
- 34 W. Cao, L. He, W. Cao, X. Huang, K. Jia and J. Dai, *Acta Biomater.*, 2020, **112**, 14–28.
- 35 A. Taheriazam, G. G. Y. Abad, S. Hajimazdarany, M. H. Imani, S. Ziaolhagh, M. A. Zandieh, S. D. Bayanzadeh, S. Mirzaei, M. R. Hamblin, M. Entezari, A. R. Aref, A. Zarrabi, Y. N. Ertas, J. Ren, R. Rajabi, M. D. A. Paskeh, M. Hashemi and K. Hushmandi, *J. Control Release*, 2023, **354**, 503–522.
- 36 A. Zhang, J. Chang, Y. Chen, Z. Huang, G. Alfranca, Q. Zhang and D. Cui, *Anal. Methods*, 2019, **11**, 5089–5097.
- 37 C. Meng, X. Zhi, C. Li, C. Li, Z. Chen, X. Qiu, C. Ding, L. Ma, H. Lu, D. Chen, G. Liu and D. Cui, *ACS Nano*, 2016, **10**, 2203–2213.
- 38 H.-L. Wu, C.-H. Kuo and M. H. Huang, *Langmuir*, 2010, **26**, 12307–12313.
- 39 M. S. Verma, P. Z. Chen, L. Jones and F. X. Gu, *RSC Adv.*, 2014, **4**, 10660–10668.
- 40 S. Atta, M. Beetz and L. Fabris, *Nanoscale*, 2019, **11**, 2946–2958.